Surfaces and Interfaces 81 (2026) 108451

Contents lists available at ScienceDirect

Surfaces and Interfaces

journal homepage: www.sciencedirect.com/journal/surfaces-and-interfaces

Hydrolysis synthesis of iridium oxide (IrO_x) on carbon for acidic oxygen evolution: Influence of heat-treatment on structure and electrocatalytic activity

Swapnil Sanjay Karade [a,b], Raghunandan Sharma [a,*], Saso Gyergyek [c], Per Morgen [a], Bettina Pilgaard Andersen [d], Martin Aaskov Karlsen [d], Dorthe Ravnsbæk [d], Shuang Ma Andersen [a,*]

[a] Department of Green Technology, University of Southern Denmark, Odense M 5230, Denmark
[b] Institute for Aqua Regeneration, Shinshu University, 4-17-1 Wakasato, Nagano-shi, Nagano 380-8553, Japan
[c] Department for Materials Synthesis, Jozef Stefan Institute, Jamova 39, SI-1000 Ljubljana, Slovenia
[d] Department of Chemistry, Aarhus University, Langelandsgade 140, 8000 Aarhus C, Denmark

ARTICLE INFO

Keywords:
IrOx/C
Hydrolysis
Oxygen evolution reaction
Carbon support
Stability

ABSTRACT

The development of efficient and durable oxygen evolution reaction (OER) electrocatalysts is critical for advancing proton exchange membrane water electrolyzers (PEMWEs). This study presents a nanostructured iridium oxide anchored on high-surface-area carbon (IrO_x/C) OER electrocatalyst, synthesized through ultrasonication-assisted deposition of hydrolysis-derived colloidal IrO_x nanoparticles onto the carbon support. The as-prepared IrO_x/C exhibits a mass activity exceeding five times that of unsupported benchmark commercial IrO_2, attributed to its uniform nanoparticle distribution and enhanced surface chemistry. Post-synthesis heat-treatments at two different temperatures (200 or 300 °C) were employed to stabilize the catalyst structure. Notably, the sample treated at 200 °C retained 84% of its initial activity after accelerated stress testing, outperforming the commercial counterpart, which retained 67 % under identical conditions. Comprehensive structural and morphological analyses revealed that the heat-treatment increased the IrO_x particle size and decreased the Ir^{3+}/Ir^{4+} ratio while leaving the amorphous nature of IrO_x unaffected, which combinedly led to the improved durability. These findings offer valuable insights into designing stable low-iridium OER electrocatalysts for acidic PEMWE applications.

1. Introduction

The transition to sustainable energy systems necessitates efficient methods for hydrogen production, with polymer electrolyte membrane water electrolyzers (PEMWEs) emerging as a promising technology due to their ability to generate high-purity hydrogen [1–3]. However, the widespread adoption of PEMWEs is hindered by the reliance on scarce and costly noble metal oxides, such as IrO_2 and RuO_2, which serve as electrocatalysts for the oxygen evolution reaction (OER) under acidic conditions [4–8].

Efforts to enhance the performance of OER electrocatalysts have focused on reducing kinetic overpotentials and minimizing catalyst loading. Strategies include optimizing the utilization of active sites to increase mass activity and modifying surface chemistry to improve intrinsic catalytic activity [9,10]. Perovskite materials have attracted attention due to their tunable structures and high intrinsic activity, yet iridium-based oxides remain preferred for their exceptional stability in harsh acidic environments [11–13].

Among iridium-based catalysts, amorphous iridium oxyhydroxide (IrOOH) and hydrated iridium oxide ($IrO_x{\cdot}nH_2O$) exhibit notable OER activity. Traditional synthesis methods, such as the alkaline hydrolysis of $[IrCl_6]^{2-}$, yield colloidal suspensions of $IrO_x{\cdot}nH_2O$ nanoparticles. While these colloids can be stabilized with surfactants or capping agents, challenges persist in producing agglomeration-free nanoparticulate powders suitable for electrode fabrication, as uncontrolled precipitation often occurs during synthesis [14].

To address these issues, supporting electrocatalyst nanoparticles on high-surface-area, conductive materials has been explored [15–17].

* Corresponding authors.
E-mail addresses: rash@igt.sdu.dk (R. Sharma), mashu@igt.sdu.dk (S.M. Andersen).

https://doi.org/10.1016/j.surfin.2026.108451
Received 24 June 2025; Received in revised form 6 December 2025; Accepted 7 January 2026
Available online 8 January 2026

Carbon black, despite its susceptibility to corrosion under oxidative conditions, is frequently used in proof-of-concept catalyst development studies due to its favorable surface area, conductivity, and porosity [18–20]. Supporting catalysts on carbon can mitigate agglomeration and enhance mass activity through improved dispersion and potential electronic interactions between the catalyst and support [21,22].

Nevertheless, supported catalysts often face stability challenges, particularly due to the inverse relationship between activity and durability in iridium-based OER catalysts [23,24], Thermal treatments have been employed to enhance stability, with studies indicating that moderate heat-treatments can influence the amorphous-to-crystalline phase transition in iridium oxides, thereby affecting catalytic performance [25]. However, the effects of low-temperature heat-treatments (below 400 °C) on supported IrO_x catalysts remain underexplored [26].

In this study, we investigate the impact of heat-treatment at temperatures ranging from 200 °C to 300 °C on the structural and electrochemical properties of IrO_x nanoparticles supported on carbon. Building upon our previous work involving ultrasonication-assisted deposition of IrO_x onto carbon supports and subsequent microwave treatments to enhance stability, we aim to elucidate the relationship between heat-treatment conditions, catalyst structure, and OER performance.

2. Materials and methods

2.1. Materials

Analytical grade iridium trichloride hydrate ($IrCl_3{\cdot}nH_2O$), sodium hydroxide (NaOH), and nitric acid (HNO_3 65 v/v %) were purchased from Sigma Aldrich and used without further purification. High purity perchloric acid ($HClO_4$; 70 % Suprapur®, Sigma-Aldrich) used as an electrolyte. Isopropanol (99.5 %, Sigma Aldrich) and a 5 wt. % solution of Nafion® (D521, IonPower) were used for preparation of the electrocatalyst ink. Ultrapure water (milliQ; resistivity $\geq$ 18.2 MΩ cm at 25 °C) was used as a solvent for preparation of the aqueous solutions for synthesis and/or electrochemical characterizations. Commercially available IrO_2 powder purchased from Alfa Aesar was used as a reference benchmark for assessment. High surface area carbon, Ketjenblack EC600JD (KB600), having a specific surface area of ~1400 m^2/g, was used as the electrocatalyst support.

2.2. Preparation of IrO_x colloidal nanoparticles

The synthesis process of IrO_x particles in colloidal form was performed as described elsewhere [26]. In brief, $IrCl_3$ solution (25 mL; 10 mM) in ultrapure water was hydrolyzed through adjusting the pH to 13 by addition of 2.5 M NaOH aqueous solution followed by stirring for 30 min at a temperature of 90 °C. In the next step (acid-condensation), the hydrolyzed solution was cooled in an ice bath before the pH was adjusted to 1.0 by using 3 M HNO_3. The solution was then stirred further for 90 min under ice bath cooling. No precipitate was observed during the acid condensation reaction and the resultant blue colloidal solution containing IrO_x nanoparticles remained stable for at least one month when stored at 2 °C.

2.3. Carbon supported IrO_x nanoparticles

For loading on the IrO_x nanoparticles from the colloidal solution on the carbon support, required amount of KB600 carbon was added the solution (target Ir loading: 20 wt. %), after adjusting the pH to 5 by means of NaOH (2.5 M aqueous solution) addition. Uniform dispersion of the carbon support in the solution was achieved by ultrasonic homogenization (10 min; 100 W) with Hielscher UP200 St ultrasonic homogenizer. The product obtained-carbon supported IrO_x (IrO_x/C hereafter)—was separated from the mother liquid by centrifugal separation followed by washing with ultrapure water to attain a neutral pH and dried in a vacuum oven held at 60 °C. Furthermore, Ir concentration in the supernatant was measured using a Thermo Scientific Niton XL3t GOLDD+*X*-ray florescence (XRF) spectrometer. Although the target Ir loading was set to 20 %, the presence of Ir in the supernatant suggested that either not all the Ir precursor gets converted to the final product IrO_x or some of the IrO_x does not land on the carbon support. The Ir content measurement in the supernatant was used to determine the reaction conversion efficiency [27], which was fond to be ~85 % in this case. Finally, the effect of heat-treatment was studied by heat-treatment of the IrO_x/C samples at different temperatures (200 °C or 300 °C) for 1 h in air with an ambient pressure (heating/cooling rates: 10 °C min^{-1}). The heat-treated samples were named as IrO_x/C-200 °C and IrO_x/C-300 °C, respectively for the heat-treatment temperatures of 200 °C and 300 °C.

2.3. Structural characterizations

The morphology of freshly synthesized IrO_x/C electrocatalysts was characterized using a JEOL JEM-2100 TEM operating at 200 kV, outfitted with a JED 2300 EDS analyzer. Total scattering measurements were carried out using a STOE STADI P diffractometer fitted with a MYTHEN 4 K detector and using Ag Kα radiation (λ = 0.559407 Å). Samples were contained in 1.1 mm Kapton® capillaries, while the commercial reference sample was placed in a 0.4 mm glass capillary. Each dataset was acquired in moving-mode over a 24-h period. The acquired scattering data were transformed into pair distribution functions using PDFgetX3 software, applying a $Q_{max\text{-}inst}$ of 19.5 $Å^{-1}$ for the reference sample. For the synthesized materials, a reduced Q_{max} of 13.0 $Å^{-1}$ was employed to suppress noise. The polynomial correction (r_{poly}) and minimum Q (Q_{min}) parameters were set to 1.5 Å and 0.1 $Å^{-1}$, respectively. Structural modeling and refinement were performed using PDFgui, fitting parameters including scale factor, unit cell dimensions, the correlated motion parameter, and average spherical domain size.

Thermogravimetric and differential scanning calorimetry measurements were conducted on a NETZSCH STA 449 F1 Jupiter instrument under a steady flow of artificial air (20 vol % O_2 / 80 vol % N_2) at 20 mL/min. The evolution of surface chemical states in the Ir-Oxide was probed via X-ray photoelectron spectroscopy using a SPECS® system with a PHOIBOS analyzer and Mg Kα radiation (1253.6 eV). Survey scans were collected over kinetic energies of 200–1200 eV at 0.5 eV steps with a 50 eV pass energy. Following this, high-resolution scans focused on specific core levels (narrow scans) were recorded with 0.1 eV resolution at 25 eV pass energy. Binding energy calibration was done by aligning the C 1 s signal (C–C bonds) to 284.7 eV. Elemental quantification utilized a "smooth" background subtraction in CasaXPS, and deconvolution of Ir 4f peaks was performed as described in the Results section. Powder XRD patterns were recorded using a Rigaku Miniflex 600 diffractometer with Cu Kα radiation (λ = 1.5418 Å). Data collection spanned 2θ angles from 30° to 80° at a scan rate of 3° per minute.

2.5. Electrochemical measurements

An electrocatalyst ink was prepared by dispersing 10 mg of catalyst powder into 5 mL of a stock mixture composed of isopropanol, water, and Nafion® in a volumetric ratio of 20:78.6:1.4. The mixture was ultrasonicated for 60 s using a Hielscher UP200St ultrasonic homogenizer to ensure thorough dispersion. A glassy carbon rotating disc electrode (GC RDE, tip diameter 5 mm) was then coated by drop-casting a 10 μL aliquot of this ink onto its surface. To promote even distribution and adherence, the electrode was rotated at 700 rpm at ambient temperature during the drying phase. Finally, the loading of iridium (Ir) and by extension, IrO_x on the electrode was quantified directly using calibrated X-ray fluorescence (XRF) measurements [28]. By directly quantifying the iridium (Ir) loading via XRF, uncertainties related to synthesis, ink formulation, and deposition techniques were effectively bypassed. This quantified Ir content, measured prior to electrochemical testing, was used to normalize the current by Ir mass, allowing for

accurate activity comparisons. The catalyst-coated glassy carbon rotating disc electrode (GC RDE) served as the working electrode within a standard three-electrode configuration, paired with a platinum wire counter electrode and a double-junction Ag/AgCl reference electrode (double junction; saturated KCl). All applied potentials were referenced to the reversible hydrogen electrode (RHE). Electrochemical measurements were performed using a ZahnerIM6e electrochemical workstation, where a positive feedback iR compensation was used to account for ~70 % of the measured iR drop (measured series resistance: ~2.8 Ω) [29]. All the measurements were performed at room temperatures using the iR compensation constant. The oxygen evolution reaction (OER) performance both in terms of catalytic activity and durability was evaluated using cyclic voltammetry in an N_2-saturated 0.1 M perchloric acid ($HClO_4$) electrolyte. An electrocatalyst-coated glassy carbon rotating disk electrode (GC RDE) was deployed at a consistent rotation speed of 1600 rpm to promote uniform mass transport. Prior to measuring activity, the electrode underwent an activation process consisting of 20 CV cycles between 1.00 and 1.70 V (vs. RHE) at a scan rate of 100 mV s^{-1}, this step helps achieve a stable electrochemical surface. After activation, two additional CVs were recorded within a narrower potential window of 1.00–1.65 V at a slower scan rate of 10 mV s^{-1}. The anodic current at 1.65 V during the second sweep was taken as the benchmark for initial OER activity. To assess longevity, the electrode was subjected to 1000 retention cycles (AST) between 1.00 and 1.70 V at 100 mV s^{-1}. After predetermined intervals within this aging protocol, intermittent observational voltammograms were recorded for two CV cycles spanning 1.00 to 1.65 V at 10 mV s^{-1}. These check-in measurements provided updated readings of OER activity, again using the second anodic sweep as the representative metric. Tracking activity against the number of stress cycles allowed for effective evaluation of performance degradation.

2.6. Post-AST structural analysis

After the electrochemical study, Ir loading on the GC RDE was again measured using XRF. As no physical detachment of the electrocatalyst layer from the GC RDE was observed, the Ir loss ($w_i - w_f$; with w_i and w_f being the values of initial and final Ir loadings on the GC RDE, was assigned to the dissolution loss (l_d) during electrochemical treatment, which is calculated using Eq. (1).

$$l_d(\%) = \frac{w_i - w_f}{w_i} \times 100 \quad (1)$$

Further, the post-AST electrocatalyst sample from the GC RDE tip was analyzed using TEM imaging.

3. Results and discussion

3.1. PDF analysis

The PDFs from the temperature series of the IrO_x samples (Fig. 1 and Fig. S1) are highly similar. The structure of the samples cannot be assigned to Ir-metal (space group F*m*-3*m*), to cubic IrO_2 (space group P*a*-3), to tetragonal IrO_2 (space group $P4_2/mnm$), or to trigonal IrOOH (space group P-3*m*1). However, the tetragonal IrO_2 and trigonal IrOOH phase could explain some bonds at short interatomic distances. Hence, even though it is not possible to resolve the structure of the samples, the results could indicate that they contain small domains with structural motifs resembling tetragonal IrO_2 and trigonal IrOOH. We note that adjusting the tetragonal IrO_2 to an orthorhombic or a monoclinic structure (as for the commercial sample) also does not improve the match towards the data.

The first correlation peak at ~2 Å is assigned to the shortest Ir-O distance. The following two correlations at 2.53 and 3.10 Å are assigned to two different O—O distances, and the fourth peak at 3.67 Å corresponds to the shortest Ir-Ir distance. The following correlation peaks are difficult to assign as several atomic distances overlap as *r* increases. The coherent domain size is evaluated to ~12 Å, i.e., the samples are highly disordered or amorphous.

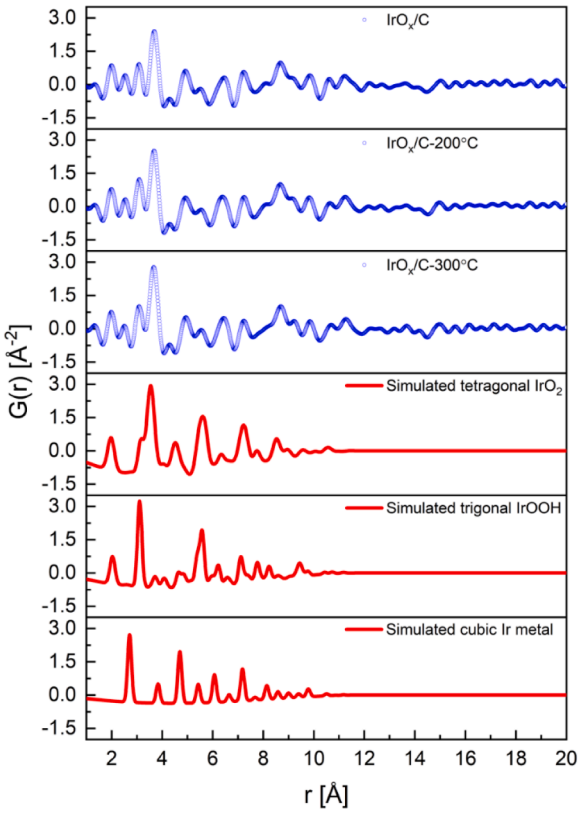

Fig. 1. PDF data of temperature series of IrO_x samples: IrO_x/C (blue, top), IrO_x/C-200 °C (blue middle), and IrO_x/C-300 °C (blue, bottom) together with simulated PDFs of tetragonal IrO_2 (red, top), trigonal IrOOH (red, middle), and cubic Ir metal (red, bottom).

3.2. Thermogravimetric analysis

The thermal stability of the synthesized iridium oxide supported on carbon (IrO_x/C) was evaluated using TGA and DSC over a temperature range of 30–900 °C. As depicted in Fig. 2a, an initial mass loss of approximately 9 % was observed up to 90 °C, attributed to the desorption of adsorbed moisture. The DSC curve exhibited a minor exothermic peak near 230 °C, likely corresponding to the decomposition of hydroxyl and hydrated groups. Based on these observations, heat-treatment temperatures of 200 °C and 300 °C were selected to investigate their effects on the electrocatalytic activity [30]. A pronounced mass loss occurred above 400 °C, indicative of the combustion of the carbon support. At 900 °C, the residual mass was approximately 23 %, aligning with the anticipated iridium oxide (IrO_2) content following oxidative removal of carbon. This residual mass corresponds well with the expected iridium loading of ~20 %, considering: (i) the targeted iridium-to-carbon molar ratio of 20:80, (ii) a measured carbonization efficiency (η_c) of ~85 %, and (iii) an iridium content of ~86 % by weight in the TGA residue. The slight discrepancy between the expected and observed residual masses may stem from experimental uncertainties inherent in the synthesis and measurement processes.

3.3. X-ray photoelectron spectroscopy

Fig. 2b shows the XPS survey spectra of the IrO_x/C, IrO_x/C-200 °C and IrO_x/C-300 °C samples, exhibiting peaks corresponding to Ir 4f, C 1 s

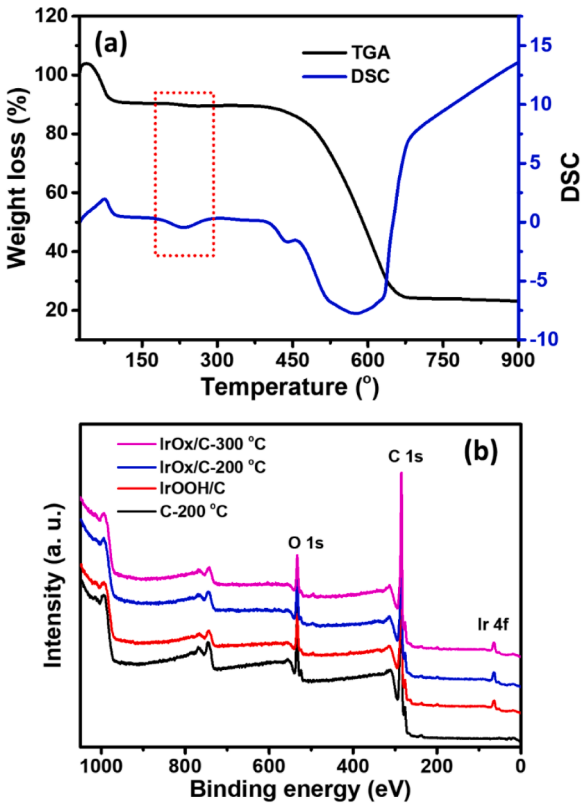

Fig. 2. (a) TGA and DSC plots of the as-synthesized IrO_x/C electrocatalyst, (b) Survey scan XPS spectra for as-synthesized and heat-treated IrO_x/C samples. XPS spectrum of the support carbon is also shown for comparison. XPS spectrum corresponding to the as-synthesized IrO_x/C electrocatalyst is reproduced from our earlier study (Ref. [26]; Creative Commons CC-BY license; Copyright 2024, Elsevier).

and O 1 s, indicating the presence of IrO_x nanoparticles coated on the surface of carbon along with lattice oxygen of IrO_x and the surface-bound oxygen on the carbon samples. The Ir 4f peak intensity appears small due to the low Ir:C (20:80) ratio. For comparison, a XPS spectrum of the support carbon sample heat-treated at 200 °C (labeled as C-200 °C) has also been shown.

In order to investigate the surface chemical states of the IrO_x/C, IrO_x/C-200 °C and IrO_x/C-300 °C samples, high resolution XPS spectra corresponding to the Ir 4f and O 1 s orbitals are analyzed as shown in Fig. 3. Although deconvolution of the Ir 4f spectra can be quite complex due to asymmetric line shapes and presence of satellite peaks [29,31,32], here we used Functional Lorentzian (LF) line shape to deconvolute the peak components. It is noted that the peak shapes resemble well with those for the hydrated IrO_2, as explored by Freakley et al. [32] and can be deconvoluted as a single pair of the Ir $4f_{7/2}$ and $4f_{5/2}$ spin-orbit components. As can be seen in Fig. S2 (supporting information), the peak deconvolution can be achieved assuming only a single oxidation state, a spin-orbital splitting of 3.0 eV along with the peak intensities constrained to their multiplicity. As the XPS spectra for all the samples appear similar, the fitting assuming single oxidation state shows that with increasing the heat-treatment temperature, the BE shifts to a value lower than that for the as-synthesized sample. For example, BE values of the Ir $4f_{7/2}$ component for the IrO_x/C, IrO_x/C-200 °C and IrO_x/C-300 °C samples are 62.1 eV, 61.9 eV and 61.8 eV, respectively. This small shift in the BE values may be attributed to (i) an electrocatalyst-support interaction or (ii) a change in the oxidation state, which was not considered during the fitting. The first possibility was discarded since the Ir $4f_{7/2}$ BE for an unsupported IrO_x sample, prepared similarly and heat-treated at 200 °C (IrO_x-200 °C), is 61.9 eV, identical to that for the corresponding supported sample (IrO_x/C-200 °C), as shown in Fig. S3, (supporting information).

Therefore, the XPS spectra of the supported samples have contributions from (at-least) two different oxidation states, and hence, the Ir $4f_{7/2}$ and $4f_{5/2}$ peaks observed in each spectrum were deconvoluted in two components each, by fixing the $4f_{7/2}$ BE values at 61.5 eV and 62.3 eV for the lower and higher BE components, assigned respectively to Ir^{4+} and Ir^{3+} oxidation states. Such a deconvolution reveals a decrease in the Ir^{3+}/Ir^{4+} ratios for the heat-treated samples (as compared to the as-synthesized one), as demonstrated in Fig. 3(a-c) and in Table 1.

Figs. 3(d-f) show the results of the deconvolution analysis of the O 1 s XPS peak from the samples studied. The O 1 s peak in the synthesized IrO_x samples has three components corresponding to Ir-O, Ir-OH and H_2O (in hydrated IrO_x) [32,33], along with two components corresponding to the *C* = *O*/C—OH and C—O-C bonds from the support carbon [34]. Here, it is noteworthy that the H_2O peak may correspond to both the C-bound and Ir-bound H_2O. .Based on this, all O 1 s spectra are deconvoluted into five components. Here, the *C* = *O*/C—OH and C—O-C components, the most abundant ones due to high content of carbon (Ir/*C* = 20:80 w/w), were fitted at constant BE values of 532.9 eV (*C* = *O*/C—OH) and 534.3 eV (C—O-C), obtained from the O 1 s spectrum of bare carbon sample (Fig. S4, supporting information). Further, for the components corresponding to Ir, LF(0.3,1.5, 25,150) line shape was used for Ir-O and Ir-OH, while the other components (H_2O, *C* = *O*/C—OH and C—O-C) were fitted using GL(30) line shape. Further, assuming the Ir-O and Ir-OH components in the O 1 s spectra correspond respectively to the Ir^{4+} and Ir^{3+} components in the Ir 4f spectra, the Ir-O to Ir-OH intensity ratio was constrained to be equal to the Ir^{4+}/Ir^{3+} ratio obtained from the Ir 4f spectra. Table 1 summarizes the relative abundance of the O 1 s peak components, showing decreasing H_2O fractions with increasing heat-treatment temperatures. It is also noteworthy that while the Ir-O to Ir-OH intensity ratio is constrained to that of the to the Ir^{4+} and Ir^{3+} components in the Ir 4f spectra, the Ir-OH fraction estimated using O 1 s spectra remain unaffected by the thermal treatment, whereas the Ir-O contribution increases with heat-treatment.

3.4. Morphological study

The morphology and size distribution of IrO_x nanoparticles supported on carbon (IrO_x/C) were investigated using TEM. Figs. 4a and 4b display TEM images of the as-synthesized IrO_x/C and the IrO_x/C sample subjected to heat-treatment at 200 °C (IrO_x/C-200 °C), revealing a uniform dispersion of IrO_x nanoparticles across the carbon support without noticeable agglomeration. Figs. 4c and 4d present the corresponding particle size distribution histograms, respectively for the IrO_x/C and IrO_x/C-200 °C samples, where the particle size analysis was conducted using the ImageJ software, measuring 50 nanoparticles selected from various regions of the TEM images. The analysis determined an average particle diameter of 1.0 ± 0.2 nm and 1.2 ± 0.2 nm, respectively for the IrO_x/C and IrO_x/C-200 °C samples, which is in close agreement with similarly sized IrO_x nanoparticles synthesized via microwave-assisted polyol methods, where average diameters of ~1.1–1.2 nm have been reported [35,36]. After the heat-treatment, the nanoparticles remain well-dispersed on the carbon substrate; however, slight agglomeration is observed, accompanied by a modest increase in average particle size. Selected area electron diffraction (SAED) patterns, corresponding to the samples IrO_x/C and IrO_x/C-200 °C, shown as insets in the corresponding TEM images, exhibit three broad diffuse rings corresponding to d-spacings of approximately 3.30, 2.20 Å and 1.26 Å nm, respectively for the inner, middle and outer rings. These spacings correspond to the diffractions from the support carbon., suggesting that the carbon support comprises few-layer graphene structures with some degree of wrinkling or twisting [37]. The absence of sharp diffraction spots or rings attributable to crystalline IrO_x or IrO_2 confirms the amorphous nature of the IrO_x phase in both the as-synthesized and heat-treated samples, indicating that the applied thermal treatment at

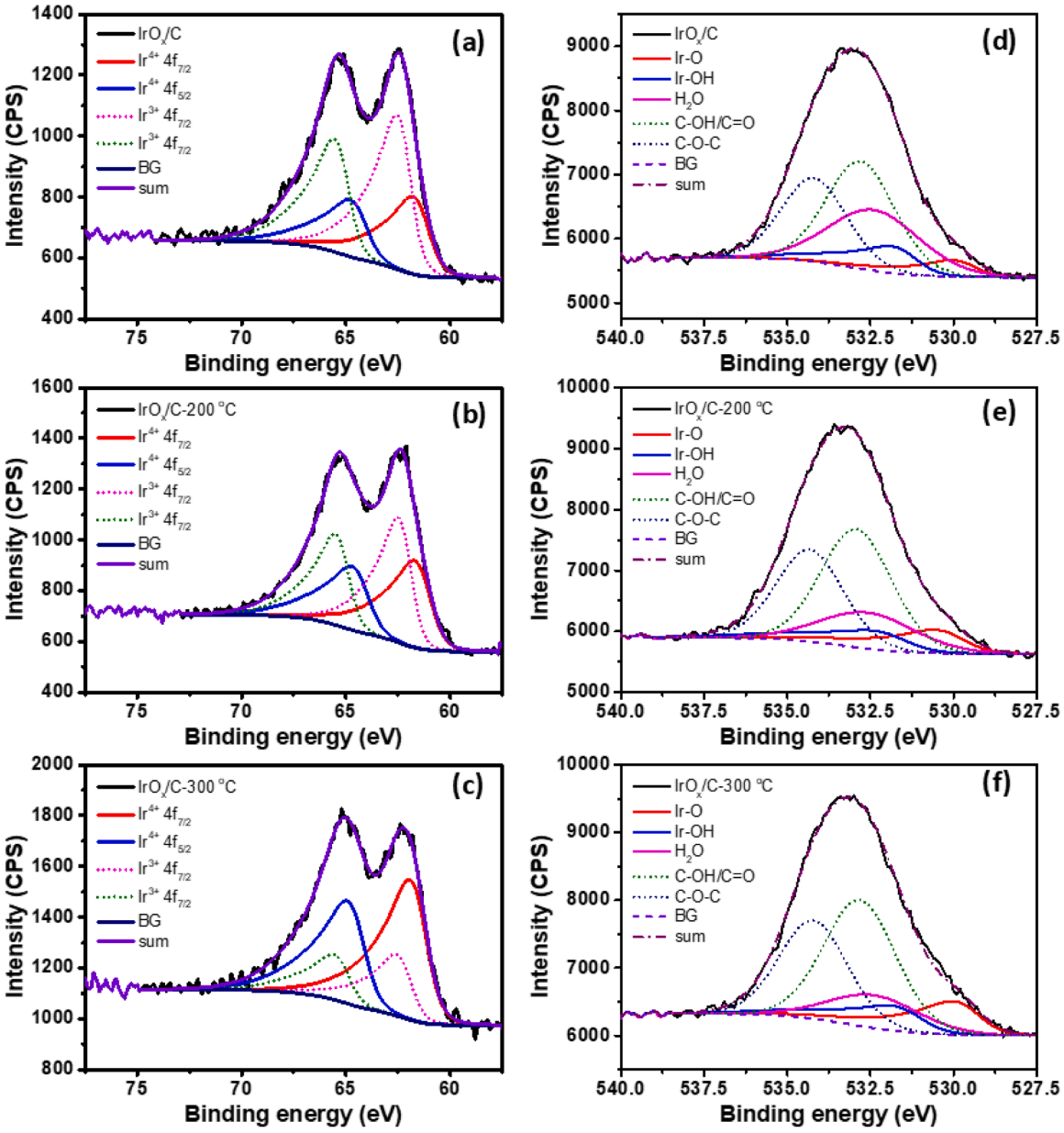

Fig. 3. XPS narrow scan spectra of (a-c) Ir 4f and (d-f) O1s for IrO_x/C, IrO_x/C-200 °C, and IrO_x/C-300 °C samples. XPS spectra shown in (a) and (d) are reproduced from our earlier study (Ref. [26]; Creative Commons CC-BY license; Copyright 2024, Elsevier).

Table 1
Peak fitting parameters of the XPS narrow scan Ir 4f and O 1 s components associated with the IrO_x/C, IrO_x/C-200 °C, and IrO_x/C-300 °C samples.

Sample	Ir 4f components					O 1 s peak components (area %)				
	BE for $4f_{7/2}$ (eV)		Area %		Ir^{3+}/Ir^{4+} ratio					
	Ir^{4+}	Ir^{3+}	Ir^{4+}	Ir^{3+}		Ir-O	Ir-OH	H_2O	C-OH/C = O	C—O—C
IrO_x/C	61.5	62.3	36.2	63.8	1.76	5.3	9.3	25.8	34.2	25.3
IrO_x/C-200 °C	61.5	62.3	53.2	46.8	0.88	9.5	8.3	15.8	38.2	28.2
IrO_x/C-300 °C	61.5	62.3	55.0	45.0	0.82	11.3	9.2	12.7	38.4	28.4

200 °C does not induce crystallization of the IrO_x nanoparticles. Besides, Fig. S5 shows TEM images of the commercial IrO_2 sample, revealing agglomerates of IrO_2 nanoparticles with irregular shape and size, with no distinguishable individual particles visible, unlike in case of the as-synthesized and heat-treated IrO_x/C samples, where the IrO_x particles remain distinct on the support carbon. In addition, XRD patterns of the commercial IrO_2 and the synthesized IrO_x/C samples shown in the Fig. S6 show subtle differences. The commercial IrO_2 sample exhibits distinct reflections at 2θ values of 40.9°, 46.7°, and 69°, corresponding to the (111), (110), and (200) planes of the face-centered cubic structure of metallic Ir. In contrast, the XRD patterns of the IrO_x/C, IrO_x/C-200 °C and IrO_x/C-300 °C samples display no discernible Bragg reflections, indicating an amorphous nature of the IrO_x phase on the surface of carbon, in agreement with the observed short-range order (small

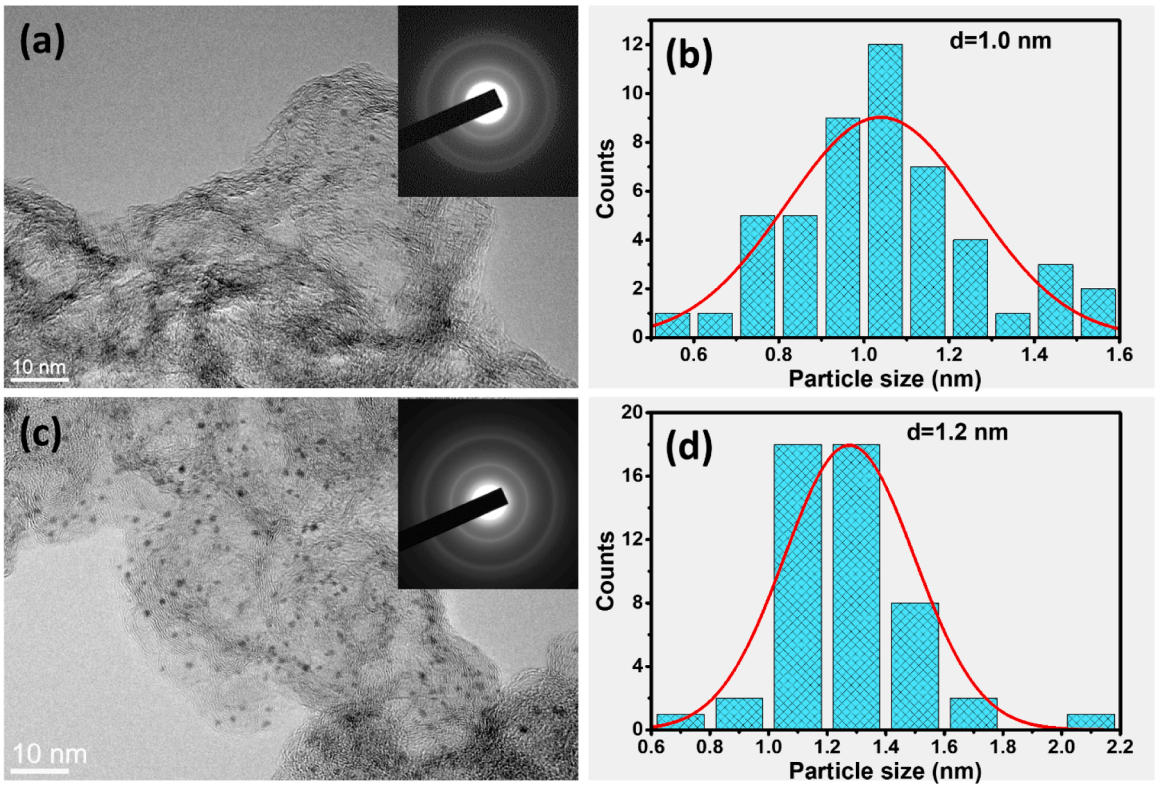

Fig. 4. TEM images of (a) IrO_x/C and (b) IrO_x/C-200 °C samples. Corresponding particle size distribution histograms are shown in (c) and (d), respectively for the IrO_x/C and IrO_x/C-200 °C samples. Insets of (a) and (b) show the corresponding SAED patterns. The three diffuse rings in the SAED patterns are assigned to the graphite carbon (space group: $P6_3mc$, having short range graphitic order (Inner ring: (002); middle ring: (101); outer ring: (110)). The indices are omitted in the SAED image for clarity.

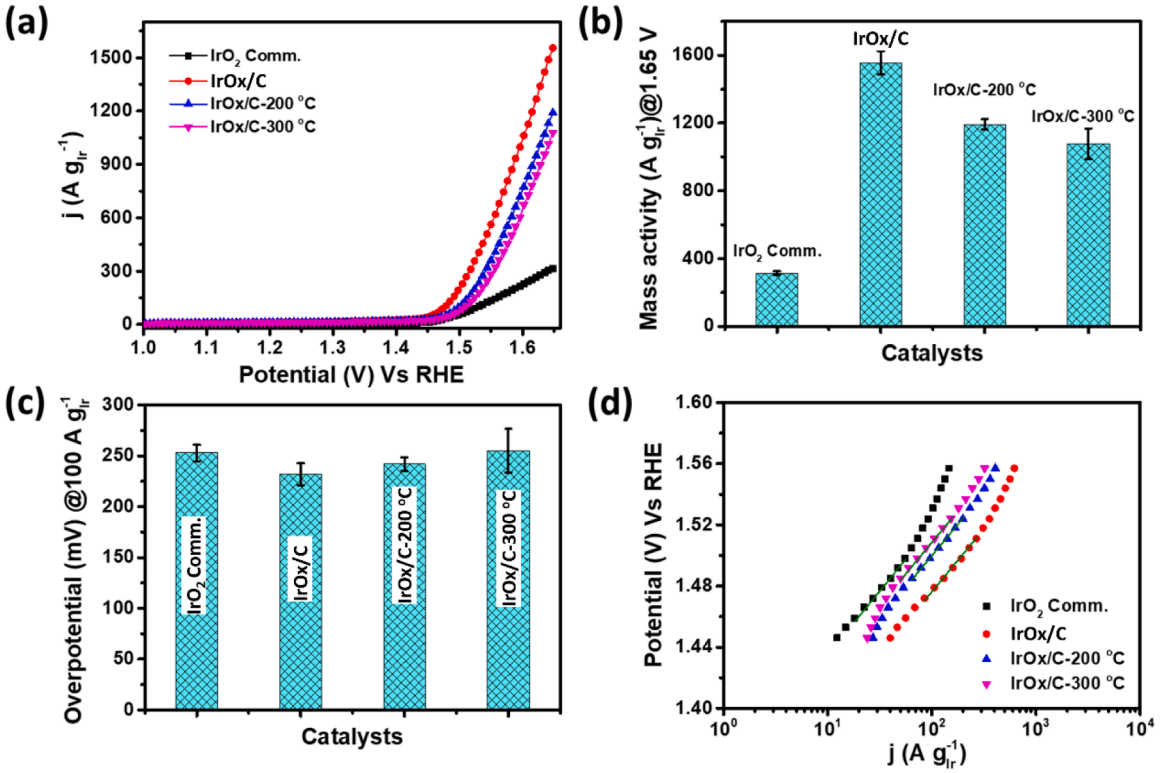

Fig. 5. Electrochemical study (a) OER polarization curve, (b) Mass activity at 1.65 V (c) Overpotential and (d) Tafel plot for IrO_x/C, IrO_x/C-200 °C and IrO_x/C-300 °C samples. Data for the sample IrO_x/C reproduced from our earlier study (Ref. [26]; Creative Commons CC-BY license; Copyright 2024, Elsevier).

coherent domain size) through detailed PDF analysis.

3.5. OER activity

Fig. 5a presents the polarization curves of the as-prepared IrO_x/C, IrO_x/C-200 °C, IrO_x/C-300 °C, and commercial IrO_2 electrocatalysts, recorded in argon-saturated 0.1 M $HClO_4$ at room temperature with a scan rate of 10 mV s^{-1}. Each catalyst was applied with a consistent total loading of 20 μg, ensuring uniform iridium content across the carbon-supported samples. The commercial IrO_2, however, possesses a different iridium content due to its distinct composition. As depicted in Fig. 5b, the mass activity defined as the current normalized to the mass of iridium at 1.65 V vs. RHE of the as-synthesized IrO_x/C surpasses that of commercial IrO_2 by more than fivefold. This enhancement can be attributed to several factors such as, (i) the smaller size of the synthesized IrO_x nanoparticles compared to that of the commercial IrO_2 (detailed characterization of the commercial IrO_2 can be found in our previous study [29], (ii) the carbon support facilitates uniform dispersion of IrO_x nanoparticles, minimizing agglomeration and maximizing active surface area and (iii) the as-synthesized IrO_x possesses a hydrated structure, promoting efficient proton-coupled electron transfer essential for OER. Comparatively, previous studies have reported up to tenfold increase in mass activity for IrO_x/C synthesized via the polyol method [25]. Despite utilizing a higher surface area carbon support (KB600, specific surface area (SSA) measured by nitrogen adsorption through Brunauer-Emmett-Teller (BET) method: 1410 m^2 g^{-1}) in our study, the observed enhancement is lower. This discrepancy may stem from differences in intrinsic activity or catalyst-support interactions inherent to the synthesis methods. Notably, appreciable mass activities at the thermoneutral potential (1.48 V vs. RHE) are observed for the IrO_x/C samples. However, absolute current values below this potential remain low and comparable across all the samples (Fig. S7). Further, heat-treatment impacts the electrocatalytic performance as IrO_x/C-200 °C sample exhibits a reduction (~23 %) in mass activity compared to the as-synthesized sample, likely due to minor particle growth and the reduced Ir^{3+}/Ir^{4+} ratio. Further, IrO_x/C-300 °C sample shows a more pronounced decrease in the initial OER activity (~31 % reduction), correlating with the further decrease in the Ir^{3+}/Ir^{4+} ratios (Table 1).

Despite the reduction, both heat-treated samples maintain mass activities higher than that of the commercial IrO_2. Fig. 5c illustrates the overpotentials required to achieve a mass activity of 100 A g_Ir^{-1}. The as-synthesized IrO_x/C demonstrates the lowest overpotential, indicating superior catalytic efficiency. Tafel analysis (Fig. 5d) reveals that IrO_x/C-200 °C possesses the smallest Tafel slope (87 mV dec^{-1}), suggesting favorable reaction kinetics. Ultimately, the initial OER activity and associated electrochemical parameters are influenced by nanoparticle size and surface hydroxide content. The as-synthesized IrO_x/C, with its minimal particle size (~1.0 nm) and hydrated structure, offers optimal performance. Heat-treatments induce particle growth and alter the surface chemistry, leading to reduced activity, yet the catalysts remain more active than commercial IrO_2.

To gain further insights into the sources of the observed reduction in OER activity due to heat-treatment, specific surface area (SSA) values of IrO_x/C electrocatalysts ($A_{IrO_x/C}$) were estimated using the rule of mixture, as their SSA measurements through nitrogen adsorption isotherms were not feasible due to small amounts of the samples available. For the calculations, SSA of support carbon (A_C), i.e., 1410 m^2 g^{-1} (measured by nitrogen adsorption isotherm, BET method) was assumed to be not affected by the electrocatalyst synthesis process. Further, to calculate the SSA of the IrO_x NPs (A_{IrO_x}), a spherical shape with the radius (R) being half of the average particle size determined from TEM analysis, is assumed. Hence, A_{IrO_x} is given by:

$$A_{IrO_x} = 4\pi R^2 n, \tag{2}$$

with n being the number of particles per unit mass (Eq. (3)).

$$n = \frac{3}{4\pi R^3 d}, \tag{3}$$

with d being the density of the particles.

Combining Eqs. (2) and 3,

$$A_{IrO_x} = \frac{3}{Rd}. \tag{4}$$

Again, the specific area of projection for the IrO_x NPs ($A^P_{IrO_x}$), i.e., the area of the support carbon covered by the IrO_x NPs is given by:

$$A^P_{IrO_x} = \frac{3}{4Rd}. \tag{5}$$

Further, $A_{IrO_x/C}$ can be calculated from Eq. (6), where f_{IrO_x} and f_C are the respective mass fractions of the IrO_x and C in the IrO_x/C electrocatalyst.

$$A_{IrO_x/C} = A_{IrO_x} f_{IrO_x} + A_C f_C - 2A^P_{IrO_x} f_{IrO_x} \tag{6}$$

Finally, the percentage coverage (C%) of the support by the IrO_x NPs is given by:

$$C\% = \frac{A^P_{IrO_x} f_{IrO_x}}{A_C f_C} \times 100 \tag{7}$$

The calculated values have been summarized in Table 2. It is clear that the estimated coverage of the support carbon by the IrO_x NPs is low (~2 %). Further, the total calculated SSA values of the as-synthesized and heat-treated IrO_x/C electrocatalysts are similar (~1179 m^2 g^{-1} and ~1171 m^2 g^{-1} for the IrO_x/C and IrO_x/C-200 °C samples). Also, the loss in SSA of IrO_x NPs due to growth in particle size amounts to ~17 %, which is close to the observed ~23 % reduction in the initial OER activity of the IrO_x/C-200 °C sample as compared to that of the IrO_x/C sample. However, considering large uncertainties in the particle size estimations (standard deviations: ~0.2 nm) from the TEM images, we qualitatively attribute the observed activity loss combinedly to the decreased SSA and the IrO_x surface chemical restructuring upon heating, as evidenced by the changes in Ir^{3+}/Ir^{4+} ratios from XPS, which likely influence the density of electrochemically active sites.

3.6. Stability assessment through AST/post-AST analysis

Electrocatalyst stability is quite important for the PEMWE anode electrocatalysts, subjected to highly oxidative potential, low pH, elevated temperature (80 °C), periodic start-stop cycling, etc. [38]. here, for durability assessment, the electrocatalysts were subjected to potential cycling between 1.00 and 1.70 V (versus RHE) at a scan rate of 100 mV s^{-1} for 1000 cycles [39]. Although steady-state stability test through galvanostatic polarization [25,40], may be preferred to resemble the PEMWE operation conditions during the stability test, we used potential cycling-based stability test protocol due to concerns related to corrosion [41] and/or passivation of the GC tip [42]. Again, GC was preferred over gold as the backing electrode due to the fact that under potential cycling, dissolution of gold [43,44] (and redeposition) would affect the durability assessment and increase the complexity (compared to use of a carbon-based backing electrode for the carbon supported IrO_x). The OER activity retention with respect to number of stress cycles is presented in Fig. 6 and also summarized in Table 2, while the pre-AST and post-AST polarization curves are shown in Fig. S8. While the as-synthesized IrO_x/C sample exhibits lower stability (activity retention at 1000 cycles: ~60 %) compared to that for the commercial reference (activity retention at 1000 cycles: ~77 %), the IrO_x/C-200 °C electrocatalyst shows outstanding stability with OER activity retention of ~84 % after 1000 stress cycles. Again, further increasing the heat-treatment temperature of 300 °C (IrO_x/C-300 °C) leads to a significant decrease in stability (activity retention at 1000 cycles: ~6 %).

Table 2
Estimation of physical surface area of the IrO_x electrocatalyst and the % coverage of the support carbon by the IrO_x NPs (symbols: as described in the text).

Sample	f_C	f_{IrO_x}	A_C ($m^2\ g^{-1}$)	2R (nm)	n	A_{IrO_x} ($m^2\ g^{-1}$)	$A^P_{IrO_x}$ ($m^2\ g^{-1}$)	$A_{IrO_x/C}$ ($m^2\ g^{-1}$)	C%
IrO_x/C	80	20	1410	1.0	1.63E+20	512.8	128	1179	2.3
IrO_x/C-200	80	20	1410	1.2	9.45E+19	427.4	107	1171	1.9

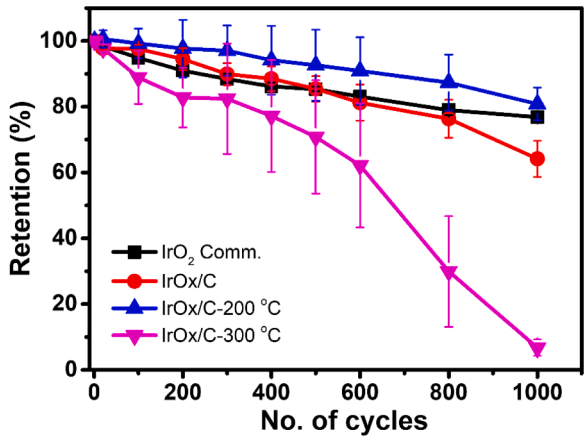

Fig. 6. OER activity evolution (retention %) along with the number of stress cycles during the AST of the IrO_2 Comm., IrO_x/C, IrO_x/C-200 °C, and IrO_x/C-300 °C electrocatalysts.

The activity degradation of Ir-based OER electrocatalysts may be attributed to several factors including (i) physical loss of the active material through dissolution and/or detachment, (ii) loss of active surface area through particle size growth, (iii) activity change due to altered surface chemistry (oxidation state of Ir, adsorbed species), etc. [45]. In a recent study in our group, it has been demonstrated that the OER activity loss during the AST (similar to that used here) for the IrO_2 commercial reference) used in this study is mainly attributed to change in the change in surface chemistry (increased oxidation state) of IrO_2, with negligible contributions from the losses due to particle growth and dissolution [29]. However, the degradation mechanisms for the synthesized IrO_x/C electrocatalyst might differ significantly as carbon is known to be unstable when exposed to high potentials such as 1.7 V and the relatively well-dispersed IrO_x nanoparticles may face severe degradation as compared to the unsupported IrO_2 commercial reference with large agglomerates. The poorer stability of IrO_x/C compared to commercial IrO_2 may be attributed to its lower structural stability and higher susceptibility to degradation under operating conditions. As-synthesized IrO_x is more prone to dissolution in acidic media compared to the more stable IrO_2 phase [46]. This can result in faster electrocatalyst degradation and loss of iridium species into the electrolyte. As evidenced by XPS analysis, the sample annealed at 200 °C exhibited improved stability compared to both the as-prepared and the 300 °C-annealed samples. This enhancement can be rationalized by the adjustment in surface oxidation states, heating at 200 °C likely promotes partial oxidation and stabilization of Ir centers, leading to a more favorable Ir^{3+}/Ir^{4+} balance that suppresses rapid surface dissolution under the potential cycling during AST. In contrast, excessive heating at 300 °C reduces the H_2O-content in the sample, leading to a decreased abundance of the electrochemically active sites and to an accelerating degradation. Table 2 summarizes the parameters associated with electrocatalysts before and after the AST cycling. The stability study provided may not adequately demonstrate the electrocatalyst's suitability for prolonged use in a PEM water electrolyzer, particularly given the concerns regarding the stability of carbon-based supports. In this context, the AST served as an efficient screening technique to distinguish between the samples analyzed, thereby illustrating the impact of heat-treatment on their stability.

To get further insights into the OER activity degradation of the synthesized IrO_x/C electrocatalysts, the post-AST samples were characterized using XRF and TEM analyses. The post-AST Ir loading on the GC RDE measured through XRF was used to estimate the loss of Ir from the electrode by dissolution during AST. As summarized in Table 3, the synthesized IrO_x/C samples show high % dissolution of Ir compared to that for the commercial IrO_2. Hence, as detailed in our previous study [29], surface chemistry change is the principal degradation mechanism for the commercial IrO_2, while for the IrO_x/C and the IrO_x/C-200 °C electrocatalysts, Ir loss due to dissolution during AST seems to play the key role in the activity loss (OER activity loss (%) ≈ dissolution (%)). On the other hand, the IrO_x/C-300 °C electrocatalyst shows an OER activity loss (95 %) significantly higher than the corresponding dissolution loss (39 %), suggesting a significant fraction of the OER activity loss due to other degradation mechanisms, i.e., particle size enlargement and/or change in surface chemistry of the electrocatalyst.

To investigate the activity degradation further, the post-AST samples of the IrO_x/C and the IrO_x/C-200 °C electrocatalysts were further analyzed through TEM analysis. Figs. 7a-d show TEM images along with particle size distributions of the post-AST IrO_x/C (Figs. 7a and 7c) and IrO_x/C-200 °C electrocatalysts (Figs. 7b and 7d), showing the respective particle size values of 1.3 ± 0.3 nm fand 1.2 ± 0.2 nm for the post-AST IrO_x/C and IrO_x/C-200 °C samples. The post-AST IrO_x/C sample shows a slight increase in particle size and hence a corresponding decrease in the specific physical surface area.

Assuming the electrocatalyst particles to be spherical, for a dissolution fraction l_d during AST, it can be shown that their pre-AST and post-AST values of PSA, respectively A_i and A_f, are related through Eq. (8), where R_i and R_f are their pre-AST and post-AST radii, respectively.

$$\frac{A_f}{A_i} = (1 - l_d) \times \frac{R_i}{R_f} \tag{8}$$

Again, relationship between the mass activity (j^m) and specific surface area (A) of an electrocatalyst can be given by Eq. (9), where U and α are the utilization factor (fraction of A contributing to the reaction) and the activity constant, respectively.

$$j^m = U\alpha A \tag{9}$$

Henec, in terms of pre-AST and post-AST mass activities, j^m_i and j^m_f, respectively, the fractional activity retention (η) can be given by Eq. (10), where subscripts i and f in the symbols correspond to pre-AST and post-AST values, respectively.

Table 3
OER activity of the studied OER electrocatalysts before and after AST cycling. Ir dissolution (%) during AST is also shown.

Sample	Cycles	Current ($A\ g_{Ir}^{-1}$)	Activity retention (%)	Activity loss (%)	Ir dissolution (%)
IrO_2 comm.	1	281	77	23	3
	1000	218			
IrO_x/C	1	1616	60	40	41
	1000	974			
IrO_x/C-200 °C	1	1239	84	16	16
	1000	1046			
IrO_x/C-300 °C	1	1079	5	95	39
	1000	54			

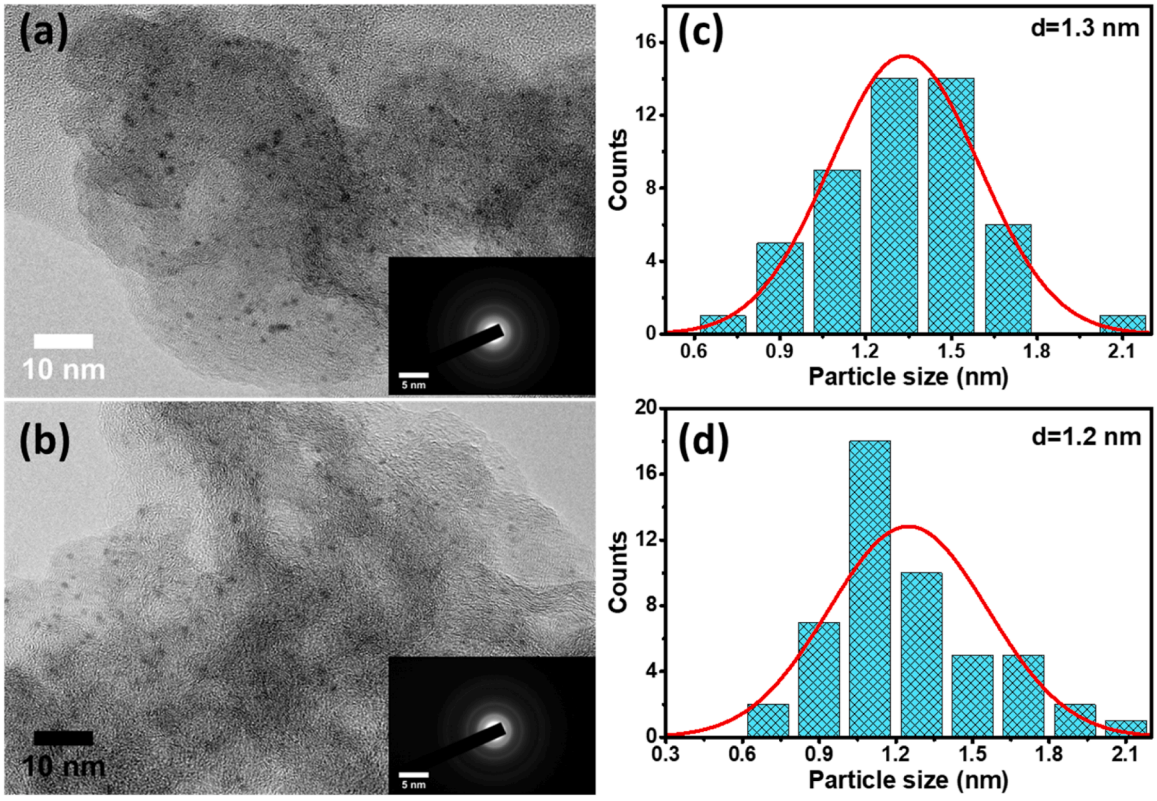

Fig. 7. TEM images and corresponding SAED patterns (inset) for the post-AST IrO_x/C and (b) IrO_x/C-200 °C samples. Corresponding particle size distributions for the IrO_x/C and IrO_x/C-200 °C samples are shown in (c) and (d), respectively.

$$\eta = \frac{j_f^m}{j_i^m} = \frac{U_f \alpha_f A_f}{U_i \alpha_i A_i} \tag{10}$$

Combining Eqs. (9) and 10 –

$$\eta = \frac{U_f \alpha_f}{U_i \alpha_i}(1 - l_d) \times \frac{R_i}{R_f} \tag{11}$$

Here, it is noteworthy that during AST, parameters U and α can decrease or increase, depending on the agglomeration state and the intrinsic activity of the electrocatalyst, respectively.

Here, for the IrO_x/C sample with l_d, R_i and R_f being 0.41, 1.0 nm and 1.2 nm and hence $A_f = 0.49A_i$, the quantity $U\alpha$ increases during the AST ($U_f\alpha_f > U_i\alpha_i$) to achieve the η value of 0.60. Possible mechanisms responsible for such a behavior could be the decreased agglomeration due to dissolution and/or increased intrinsic activity through electrochemistry-induced surface structural changes, which need further exploration. Again, despite similar physicochemical characteristics, the poorer stability of the IrO_x/C-300 °C sample compared to that of the IrO_x/C-200 °C sample may be attributed to large decrease in $U\alpha$ during AST, possibly due to surface damage of the carbon support in close vicinity of the IrO_x nanoparticles (due to their catalytic effect on thermal oxidation of carbon) during heat-treatment in air at 300 °C.

Table 4 summarizes the electrochemical performance comparison of Ir-based catalysts with different supports [47–54].

In present study IrO_x/C catalyst exhibits both high mass activity (1680 A g^{-1} Ir at 1.65 V) and improve the durability after heat-treated at 200 °C for 1 h (84 % retention over 1000 cycles) outperforming many previously reported systems, including IrO_x/ITO and Ir-IrO_x/WO_x. The conductivity and high surface area of carbon supports contribute significantly to these performance advantages. However, Ru-containing systems (e.g., $Ir_{0.5}Ru_{0.5}$/C achieving up to 2494 A g^{-1}) highlight that activity gains are possible with bimetallic designs, though often at a cost to stability. Our current work, operating under moderately acidic conditions (0.1 M $HClO_4$), delivers a practical compromise between performance and simplicity, with scalable implications.

4. Future prospectus

The current study was designed as a fundamental investigation to

Table 4
Performance comparison of Ir-based electrocatalysts with the present study.

Catalysts	Support	Method	Electrolyte	Activity	Retention stability	Ref.
IrO_x	Ni/Co-ZIF-67	Wet-chemical method	1 M KOH	50 A g_{Ir}^{-1} @ 1.55 V	-	[47]
Ir-IrO_x	WO_x	Alkaline hydrolysis	0.5 M H_2SO_4	812 A g_{Ir}^{-1} @ 1.55 V	40 % after 1000 cycles	[48]
IrO_x	ITO	Metal-organic chemical deposition	0.1 M $HClO_4$	207 A g_{Ir}^{-1} @ 1.52 V	-	[49]
Ir	ATO	Microwave assisted polyol method	0.1 M $HClO_4$	777 A g_{Ir}^{-1} @ 1.65 V	20 % after 2000 cycles	[50]
Ir	Carbon	Impregnation followed by Solid-state reduction	0.1 M $HClO_4$	1209 A g_{Ir}^{-1} @ 1.65 V	80 % after 1000 cycles	[51]
$Ru_{0.75}Ir_{0.25}O_2$	rGO	Ion exchange/activation method	0.5 M H2SO4	1941 A g_{Ir}^{-1} @ 1.66 V	-	[52]
$Ir_{0.25}Ru_{0.75}$	Carbon	Impregnation followed by solid state reduction	0.1 M HClO4	2494 A g_{Ir+Ru}^{-1} @ 1.65 V	63 % after 1000 cycles	[53]
IrO_2	TiO2	Freeze-drying method	0.1 M HClO4	52 A g_{Ir}^{-1} @ 1.65 V	-	[54]
IrO_x/C-200 °C	Carbon	Hydrolysis/Heat-treatment	0.1 M $HClO_4$	1239 A g_{Ir}^{-1} @ 1.65 V	84 % after 1000 cycles	This work

correlate synthetic parameters, heat-treatment effects, and surface chemistry with activity and stability using a half-cell configuration, which is widely employed as the first step in catalyst screening. The observed superior activity and durability of our IrO_x/C catalyst relative to commercial IrO_2 in the half-cell thus provide a strong indication of its promise. We acknowledge that future studies involving membrane electrode assembly (MEA) testing under unit cell conditions will be essential to validate its practical applicability. The working with a focus of MEA/unit cell testing with valuable support like ITO, ATO, TiO_2, and TiN, which will have future scope of studies. Faradaic efficiency (FE) would provide direct evidence to exclude possible side reactions such as carbon oxidation and to confirm that the measured current arises solely from the OER. So, there will be further scope to quantifying FE using operando gas analysis to further strengthen the understanding of catalyst selectivity along with surface chemical changes via in-situ/operando Raman characterizations.

5. Conclusions

In this study, we developed a hydrolysis–sonication approach to synthesize colloidal iridium oxide (IrO_x) nanoparticles supported on high-surface-area carbon. UV–Vis spectroscopy elucidated intermediate species during nanoparticle formation, while sonication in an ice-cold bath facilitated uniform deposition onto the carbon support. X-ray photoelectron spectroscopy revealed surface phase transformations and structural modifications induced by heat-treatment. Electrochemical evaluations demonstrated that the as-prepared IrO_x/C catalyst exhibited a mass activity exceeding five times that of commercial IrO_2. Accelerated stress tests indicated enhanced stability upon heat-treatment at 200 °C, with the IrO_x/C-200 °C sample retaining 84 % of its initial activity, compared to 60 % retention for the untreated catalyst. This improvement is attributed to alterations in surface chemistry (reduced Ir^{3+}/Ir^{4+} ratio), as no significant changes in bulk structure or domain size (~1 nm) were observed across the heat-treated samples. These findings underscore the effectiveness of controlled heat-treatment in optimizing the electrocatalytic performance and durability of IrO_x-based catalysts for acidic oxygen evolution reactions. Looking ahead, further work should focus on exploring alternative conductive supports to enhance nanoparticle anchoring and corrosion resistance and employing *in situ*/operando spectroscopic techniques to capture dynamic surface transformations under electrochemical operations. Such investigations will provide deeper mechanistic insights and guide the rational design of next-generation IrO_x-based electrocatalysts.

Supporting information

PDF data, Ir 4f XPS spectra, Ir 4f XPS spectra of unsupported IrOx-200 °C sample, O 1 s XPS spectra of support Carbon, TEM images of commercial IrO_2 sample, XRD patterns, CV curves of the electrocatalysts samples, and Pre-AST and post-AST LSV curves.

Data availability

The data will be made available on request.

Declaration of generative AI and AI-assisted technologies in the writing process

During the preparation of this work, no generative AI and AI-assisted technologies have been used.

CRediT authorship contribution statement

Swapnil Sanjay Karade: Writing – original draft, Visualization, Validation, Investigation, Formal analysis, Data curation. **Raghunandan Sharma:** Writing – review & editing, Visualization, Validation, Supervision, Project administration, Methodology, Investigation, Formal analysis, Conceptualization. **Saso Gyergyek:** Writing – review & editing, Investigation, Data curation. **Per Morgen:** Writing – review & editing, Validation, Data curation. **Bettina Pilgaard Andersen:** Writing – review & editing, Investigation, Data curation. **Martin Aaskov Karlsen:** Writing – review & editing. **Dorthe Ravnsbæk:** Writing – review & editing, Validation. **Shuang Ma Andersen:** Writing – review & editing, Visualization, Supervision, Resources, Project administration, Methodology, Funding acquisition, Conceptualization.

Declaration of competing interest

All authors declare no competing financial interest.

Acknowledgements

Authors acknowledge the financial supports from the Danish Energy Agency (EUDP project 3R, Nr. 64019–0551), the Innovation Fund Denmark (InnoExplorer program, Nr. 9122–00112), the Danish ESS lighthouse on hard materials in 3D, SOLID (Grant number 8144–00002B) the Novo Nordic Foundation (NERD Grant NNF20OC0062068) and the Energi Fyn development fund, Slovenian Research Agency (research core funding Nos. P2-0089) for this research. The CENN Nanocenter is acknowledged for the use of the Transmission Electron Microscope Jeol JEM-2100.

Supplementary materials

Supplementary material associated with this article can be found, in the online version, at doi:10.1016/j.surfin.2026.108451.

Data availability

Data will be made available on request.

References

[1] Barbir, F.J.. PEM electrolysis for production of hydrogen from renewable energy sources. 2005, 78 (5), 661–669.
[2] Carmo, M.; Fritz, D.L.; Mergel, J.; Stolten, D.J.. A comprehensive review on PEM water electrolysis. 2013, 38 (12), 4901–4934.
[3] Grigoriev, S.; Porembsky, V.; Fateev, V.J.. Pure hydrogen production by PEM electrolysis for hydrogen energy. 2006, 31 (2), 171–175.
[4] Antolini, E.J. Iridium as catalyst and cocatalyst for oxygen evolution/reduction in acidic polymer electrolyte membrane electrolyzers and fuel cells. 2014, 4 (5), 1426–1440.
[5] Danilovic, N.; Subbaraman, R.; Chang, K.C.; Chang, S.H.; Kang, Y.; Snyder, J.; Paulikas, A.P.; Strmcnik, D.; Kim, Y.T.; Myers, D.J.. Using surface segregation to design stable Ru-Ir oxides for the oxygen evolution reaction in acidic environments. 2014, 126 (51), 14240–14245.
[6] Oh, H.-S.; Nong, H.N.; Reier, T.; Bergmann, A.; Gliech, M.; Ferreira de Araújo, J.; Willinger, E.; Schlögl, R.; Teschner, D.; Strasser, P.J.. Electrochemical catalyst–support effects and their stabilizing role for IrO x nanoparticle catalysts during the oxygen evolution reaction. 2016, 138 (38), 12552–12563.
[7] Reier, T.; Oezaslan, M.; Strasser, P.J. Electrocatalytic oxygen evolution reaction (OER) on Ru, Ir, and Pt catalysts: a comparative study of nanoparticles and bulk materials. 2012, 2 (8), 1765–1772.
[8] Siracusano, S.; Van Dijk, N.; Payne-Johnson, E.; Baglio, V.; Aricò, A.J. Nanosized IrOx and IrRuOx electrocatalysts for the O2 evolution reaction in PEM water electrolysers. 2015, 164, 488–495.
[9] Nong, H.N.; Gan, L.; Willinger, E.; Teschner, D.; Strasser, P.J.. IrOx core-shell nanocatalysts for cost-and energy-efficient electrochemical water splitting. 2014, 5 (8), 2955–2963.
[10] Reier, T.; Pawolek, Z.; Cherevko, S.; Bruns, M.; Jones, T.; Teschner, D.; Selve, S.r.; Bergmann, A.; Nong, H.N.; Schlögl, R.J. Molecular insight in structure and activity of highly efficient, low-Ir Ir–Ni oxide catalysts for electrochemical water splitting (OER). 2015, 137 (40), 13031–13040.
[11] J.-W. Zhao, K. Yue, H. Zhang, S.-Y. Wei, J. Zhu, D. Wang, J. Chen, V.Y. Fominski, G.-R. Li, The formation of unsaturated IrO_x in SrIrO3 by cobalt-doping for acidic oxygen evolution reaction, Nat. Commun. 15 (1) (2024) 2928.
[12] H.M. Xu, K.H. Yue, L.J. Song, H.C. Zhang, H.R. Zhu, Z.J. Zhang, G.R. Li, The asymmetrical Fe− O− Se bonds in Fe2O (SeO3) 2 boosting bifunctional oxygen electrocatalytic performance for zinc-air battery, Angew. Chem. Int. Ed. 63 (51) (2024) e202412025.

[13] J.-W. Zhao, H. Zhang, C.-F. Li, X. Zhou, J.-Q. Wu, F. Zeng, J. Zhang, G.-R. Li, Key roles of surface Fe sites and Sr vacancies in the perovskite for an efficient oxygen evolution reaction via lattice oxygen oxidation, Energy Env. Sci. 15 (9) (2022) 3912–3922.

[14] Zhao, Y.; Hernandez-Pagan, E.A.; Vargas-Barbosa, N.M.; Dysart, J.L.; Mallouk, T.E.. A high yield synthesis of ligand-free iridium oxide nanoparticles with high electrocatalytic activity. 2011, 2 (5), 402–406.

[15] H.-S. Oh, H.N. Nong, T. Reier, A. Bergmann, M. Gliech, J. Ferreira de Araújo, E. Willinger, R. Schlögl, D. Teschner, P. Strasser, Electrochemical catalyst–support effects and their stabilizing role for IrO_x nanoparticle catalysts during the oxygen evolution reaction, J. Am. Chem. Soc. 138 (38) (2016) 12552–12563, https://doi.org/10.1021/jacs.6b07199.

[16] M. Bele, P. Jovanovič, Z.i. Marinko, S. Drev, V.S. Šelih, J. Kovač, M. Gaberščcek, G. Koderman Podboršek, G. Dražić, N. Hodnik, Increasing the oxygen-evolution reaction performance of nanotubular titanium oxynitride-supported Ir nanoparticles by a strong metal–support interaction, ACS. Catal. 10 (22) (2020) 13688–13700.

[17] X. Wu, B. Feng, W. Li, Y. Niu, Y. Yu, S. Lu, C. Zhong, P. Liu, Z. Tian, L. Chen, et al., Metal-support interaction boosted electrocatalysis of ultrasmall iridium nanoparticles supported on nitrogen doped graphene for highly efficient water electrolysis in acidic and alkaline media, Nano Energy 62 (2019) 117–126, https://doi.org/10.1016/j.nanoen.2019.05.034.

[18] Antolini, E.J. Carbon supports for low-temperature fuel cell catalysts. 2009, 88 (1–2), 1–24.

[19] Antolini, E.J.. Graphene as a new carbon support for low-temperature fuel cell catalysts. 2012, 123, 52–68.

[20] Dicks, A.L. The role of carbon in fuel cells. 2006, 156 (2), 128–141.

[21] A.G. Hufnagel, S. Häringer, M. Beetz, B. Böller, D. Fattakhova-Rohlfing, T. Bein, Carbon-templated conductive oxide supports for oxygen evolution catalysis, Nanoscale 11 (30) (2019) 14285–14293.

[22] A. Bornet, R. Pittkowski, T.M. Nielsen, E. Berner, A. Maletzko, J. Schröder, J. Quinson, J. Melke, K.M. Jensen, M. Arenz, Influence of temperature on the performance of carbon-and ATO-supported oxygen evolution reaction catalysts in a gas diffusion electrode setup, ACS. Catal. 13 (11) (2023) 7568–7577.

[23] S. Geiger, O. Kasian, B.R. Shrestha, A.M. Mingers, K.J.J. Mayrhofer, S. Cherevko, Activity and stability of electrochemically and thermally treated iridium for the oxygen evolution reaction, J. Electrochem. Soc. 163 (11) (2016) F3132, https://doi.org/10.1149/2.0181611jes.

[24] T. Reier, D. Teschner, T. Lunkenbein, A. Bergmann, S. Selve, R. Kraehnert, R. Schlögl, P. Strasser, Electrocatalytic oxygen evolution on iridium oxide: uncovering catalyst-substrate interactions and active iridium oxide species, J. Electrochem. Soc. 161 (9) (2014) F876, https://doi.org/10.1149/2.0411409jes.

[25] C. Daiane Ferreira da Silva, F. Claudel, V. Martin, R. Chattot, S. Abbou, K. Kumar, I. Jiménez-Morales, S. Cavaliere, D. Jones, J. Rozière, et al., Oxygen evolution reaction activity and stability benchmarks for supported and unsupported IrO_x electrocatalysts, ACS. Catal. 11 (7) (2021) 4107–4116, https://doi.org/10.1021/acscatal.0c04613.

[26] S. Sanjay Karade, R. Sharma, P. Morgen, R.K. Pittkowski, Ø. M, K. Jensen, S. Ma Andersen, Intrinsic oxygen evolution reaction activity and stability enhancement of IrO_x electrocatalysts by microwave irradiation, Appl. Surf. Sci. 682 (2025) 161758, https://doi.org/10.1016/j.apsusc.2024.161758.

[27] S.S. Karade, R. Sharma, M.A.B. Hedegaard, S.M. Andersen, Stepwise understanding on hydrolysis formation of the IrO_x nanoparticles as highly active electrocatalyst for oxygen evolution reaction, Electrocatalysis 15 (4) (2024) 291–300, https://doi.org/10.1007/s12678-024-00874-x.

[28] M. Chourashiya, R. Sharma, S.M. Andersen, Accurate determination of catalyst loading on glassy carbon disk and its impact on thin film rotating disk electrode for oxygen reduction reaction, Anal. Chem. 90 (24) (2018) 14181–14187.

[29] R. Sharma, P. Morgen, D. Makovec, S. Gyergyek, S.M. Andersen, Clarification of degradation mechanisms of the OER activity of Ir-based electrocatalyst with potentiodynamic accelerated stress test, J. Electrochem. Soc. 171 (7) (2024) 074514, https://doi.org/10.1149/1945-7111/ad6716.

[30] Kielbik, P.; Kaszewski, J.; Dominiak, B.; Damentko, M.; Serafińska, I.; Rosowska, J.; Gralak, M.A.; Krajewski, M.; Witkowski, B.S.; Gajewski, Z.J.N.R.L. Preliminary studies on biodegradable zinc oxide nanoparticles doped with Fe as a potential form of iron delivery to the living organism. 2019, 14 (1), 1–13.

[31] V. Pfeifer, T.E. Jones, J.J. Velasco Vélez, C. Massué, R. Arrigo, D. Teschner, F. Girgsdies, M. Scherzer, M.T. Greiner, J. Allan, et al., The electronic structure of iridium and its oxides, Surf. Interface Anal. 48 (5) (2016) 261–273, https://doi.org/10.1002/sia.5895.

[32] S.J. Freakley, J. Ruiz-Esquius, D.J. Morgan, The X-ray photoelectron spectra of Ir, IrO2 and IrCl3 revisited, Surf. Interface Anal. 49 (8) (2017) 794–799, https://doi.org/10.1002/sia.6225.

[33] Mehdipour, M.; Tabaian, S.H.; Firoozi, S.J.. Anodic electrodeposition of ligand-free iridium oxide on titanium with high mass loading and study of electrochemical treatments. 2020, 858, 113831.

[34] Sharma, R.; Gyergyek, S.; Chamier, J.; Morgen, P.; Andersen, S.M.J.C.. Pt/C electrocatalyst durability enhancement by inhibition of Pt nanoparticle growth through microwave pretreatment of carbon support. 2021, 8 (6), 1183–1195.

[35] I. Jiménez-Morales, S. Cavaliere, M. Dupont, D. Jones, J. Roziere, On the stability of antimony doped tin oxide supports in proton exchange membrane fuel cell and water electrolysers, Sustain. Energy Fuels. 3 (6) (2019) 1526–1535.

[36] I. Jiménez-Morales, J. Rozière, D. Jones, S. Cavaliere, A comprehensive activity–stability correlation study of tantalum-doped tin oxide as a support for iridium oxide in low loading water electrolysis cell anodes, RSC Appl. Interfaces (2025).

[37] Z. Czigány, L. Hultman, Interpretation of electron diffraction patterns from amorphous and fullerene-like carbon allotropes, Ultramicroscopy 110 (7) (2010) 815–819, https://doi.org/10.1016/j.ultramic.2010.02.005.

[38] Weiß, A.; Siebel, A.; Bernt, M.; Shen, T.-H.; Tileli, V.; Gasteiger, H.J.. Impact of intermittent operation on lifetime and performance of a PEM water electrolyzer. 2019, 166 (8), F487.

[39] Zhu, J.; Lyu, Z.; Chen, Z.; Xie, M.; Chi, M.; Jin, W.; Xia, Y.J. Facile synthesis and characterization of Pd@ Ir n L (n= 1–4) core–Shell nanocubes for highly efficient oxygen evolution in acidic Media. 2019, 31 (15), 5867–5875.

[40] S. Geiger, O. Kasian, A.M. Mingers, S.S. Nicley, K. Haenen, K.J.J. Mayrhofer, S. Cherevko, Catalyst stability benchmarking for the oxygen evolution reaction: the importance of backing electrode material and dissolution in accelerated aging studies, ChemSusChem. 10 (21) (2017) 4140–4143, https://doi.org/10.1002/cssc.201701523.

[41] I.A. Khan, P. Morgen, R. Sharma, S.M. Andersen, Limitations of chronopotentiometry test protocols for stability study on oxygen evolution reaction electrocatalysts and recommendations, J. Phys. Chem. C 128 (7) (2024) 2828–2833, https://doi.org/10.1021/acs.jpcc.3c07103.

[42] J. Edgington, A. Deberghes, L.C. Seitz, Glassy carbon substrate oxidation effects on electrode stability for oxygen evolution reaction catalysis stability benchmarking, ACS. Appl. Energy Mater. 5 (10) (2022) 12206–12218, https://doi.org/10.1021/acsaem.2c01690.

[43] S. Cherevko, A.A. Topalov, I. Katsounaros, K.J.J. Mayrhofer, Electrochemical dissolution of gold in acidic medium, Electrochem. Commun. 28 (2013) 44–46, https://doi.org/10.1016/j.elecom.2012.11.040.

[44] M. Zlatar, D. Escalera-López, M.G. Rodríguez, T. Hrbek, C. Götz, R. Mary Joy, A. Savan, H.P. Tran, H.N. Nong, P. Pobedinskas, et al., Standardizing OER electrocatalyst benchmarking in aqueous electrolytes: comprehensive guidelines for accelerated stress tests and backing electrodes, ACS. Catal. 13 (23) (2023) 15375–15392, https://doi.org/10.1021/acscatal.3c03880.

[45] F. Claudel, L. Dubau, G. Berthomé, L. Sola-Hernandez, C. Beauger, L. Piccolo, F. Maillard, Degradation mechanisms of oxygen evolution reaction electrocatalysts: a combined identical-location transmission electron microscopy and X-ray photoelectron spectroscopy study, ACS. Catal. 9 (5) (2019) 4688–4698.

[46] N.T.T. Thao, J.U. Jang, A.K. Nayak, H. Han, Current trends of iridium-based catalysts for oxygen evolution reaction in acidic water electrolysis, Small. Sci. 4 (1) (2024) 2300109.

[47] S. Perumal, T. Lim, S. Seenivasan, J. Seo, Electrocatalytic oxygen evolution reaction at IrO_x supported by Ni/Co-ZIF-67: controlled ratio of metallic Ir and Ir3+ states, Appl. Surf. Sci. 604 (2022) 154553.

[48] L.-Y. Chueh, C.-H. Kuo, R.-H. Yang, D.-H. Tsai, M.-H. Tsai, C.-C. Yang, H.-Y. Chen, C.-H. Wang, Y.-T. Pan, WOx nanowire supported ultra-fine Ir-IrO_x nanocatalyst with compelling OER activity and durability, Chem. Eng. J. 464 (2023) 142613.

[49] J.-A. Hoffman, Z.S. Rajan, D. Susac, M.C. Matoetoe, R. Mohamed, Influence of support physicochemical properties on the oxygen evolution reaction performance of ITO-supported IrO x nanoparticles, J. Phys. Chem. C 127 (2) (2023) 894–906.

[50] I.A. Khan, P. Morgen, S. Gyergyek, R. Sharma, S.M. Andersen, Selection on antimony-doped tin oxide (ATO) as an efficient support for iridium-based oxygen evolution reaction (OER) catalyst in acidic media, Mater. Chem. Phys. 308 (2023) 128192, https://doi.org/10.1016/j.matchemphys.2023.128192.

[51] E. Sadeghi, P. Morgen, D. Makovec, S. Gyergyek, R. Sharma, S.M. Andersen, Scalable solid-state synthesis of carbon-supported ir electrocatalysts for acidic oxygen evolution reaction: exploring the structure–activity relationship, ACS. Appl. Mater. Interfaces. 16 (40) (2024) 53750–53763.

[52] B. Zhang, C. Wen, M. Xu, Z. Ye, W. Chen, B. Chen, R. Hu, D. Wang, Z. Tu, In-situ growth of ruthenium-iridium oxides on reduced graphene oxide for acidic oxygen evolution electrocatalysis, Fuel 400 (2025) 135786.

[53] E. Sadeghi, S.Y. Kim, P. Morgen, S.B. Simonsen, M.A. Hedegaard, R. Sharma, S. M. Andersen, Solid-State approach to bimetallic IrRu/C catalysts tuning toward boosted oxygen evolution in acidic Media, ACS. Appl. Energy Mater. 8 (9) (2025) 5897–5910.

[54] S. Zargarian, C. Roiron, G. Ferro, P. Atanassov, Iridium oxide network on non-conductive TiO2 support as a catalyst for oxygen evolution reaction, ChemElectroChem. 12 (8) (2025) e202400625.